IEEE Access
Multidisciplinary | Rapid Review | Open Access Journal

Received August 25, 2019, accepted September 26, 2019, date of publication October 9, 2019, date of current version October 23, 2019.

Digital Object Identifier 10.1109/ACCESS.2019.2946374

Accurate and Efficient Segmentation of Optic Disc and Optic Cup in Retinal Images Integrating Multi-View Information

YUAN GAO[1], XIAOSHENG YU[2], CHENGDONG WU[2], WEI ZHOU[3], XIAONAN WANG[4], AND HAO CHU[2]

[1]College of Information Science and Engineering, Northeastern University, Shenyang 110819, China
[2]Faculty of Robot Science and Engineering, Northeastern University, Shenyang 110819, China
[3]School of Computing, Shenyang Aerospace University, Shenyang 110136, China
[4]College of Basic Medical Science, China Medical University, Shenyang 110122, China

Corresponding authors: Xiaosheng Yu (yuxiaosheng@ise.neu.edu.cn) and Chengdong Wu (wuchengdong@ise.neu.edu.cn)

This work was supported in part by the National Natural Science Foundation of China under Grant 61701101, Grant U1713216, Grant 61901098, Grant 61971118, and Grant 61973063, in part by the National Key Robot Project under Grant 2017YFB1301103, in part by the Fundamental Research Fund for the Central Universities of China under Grant N172603001, Grant N181602014, Grant N172604004, Grant N172604003, and Grant N172604002, in part by the Liaoning Provincial Department of Science and Technology Natural Fund Guidance Project under Grant 2019-ZD-0234, in part by the Scientific Research Fund Project of Liaoning Provincial Department of Education under Grant JYT19040, and in part by the Shenyang Research Fund Grant 18-013-0-15.

ABSTRACT Glaucoma is an eye disease which is one of the most common causes of blindness. Accurate optic disc (OD) and optic cup (OC) segmentation play a critical role for detecting glaucoma. Considering that the existing approaches can't effectively integrate the multi-view information deriving from shape and appearance to sufficiently describe OD and OC for segmentation, Locally Statistical Active Contour Model with the Information of Appearance and Shape (LSACM-AS) and Modified Locally Statistical Active Contour Model with the Information of Appearance and Shape (MLSACM-AS) are proposed in this paper. The main contributions are as below: (1) we introduce the Locally Statistical Active Contour Model (LSACM) to address the commonly occurred intensity inhomogeneity phenomenon caused by imperfection of image devices or illumination variations. (2) In order to overcome the common effects caused by pathological changes (i.e., peripapillary atrophy (PPA)) and vessel occlusion in OD and OC segmentation, we integrate the local image probability information around the point of interest from a multi-dimensional feature space into our model to preserve the integrity of the OD and OC structures. (3) Since the segmentation objects have the similar ellipse shape structure, we incorporate the shape priori constraint information into our model to further improve the robustness of the variations found in and around objects regions. To evaluate the effectiveness of the proposed models, an available publicly DRISHTI-GS database is employed in this paper. Seen from the abundant experiments, the proposed models outperform the state-of-the-art approaches in terms of the obtained qualitative and quantitative results.

INDEX TERMS Glaucoma, optic disc, optic cup, active contour model, prior information.

I. INTRODUCTION

Glaucoma is a chronic ocular disorder. It is the second biggest cause of vision loss in the world, accounting for 12.3% of entire blindness world-wide [1]. According to prediction, 80 million people will be affected by 2020 [2]. Glaucoma is asymptomatic in the early stage but gradually results in irreversible vision loss. 70%-90% of the glaucomatous patients world-wide are unaware of the disease until it has arrived its later period [1]. However, early cure can reduce the rate of blindness by about 50% as reporting in [3]. Hence early detection for glaucoma is essential.

Optic nerve head (ONH) assessment is most reliable to detect glaucoma and can be done by a trained professional. But manual assessment is time-consuming, expensive and highly subjective [4]. Therefore, automatic optic disc (OD) assessment using retinal fundus images would be very beneficial [5]. Optic disc is a bright elliptical region with a center brighter round zone called the optic cup (OC), the region located between the OD and the OC boundaries named the neuroretinal rim, as shown in Fig.1 According to the characteristics of the OD, there are two strategies for automatic

The associate editor coordinating the review of this manuscript and approving it for publication was Larbi Boubchir.

ONH assessment. One is to utilize different classification strategies for distinguishing the healthy and glaucoma fundus images. However, the main limitation in it is that this process requires a large number of labeled training samples for training model which is difficult and challenging. The other is to employ clinical indicators, such as the vertical cup to disc ratio (CDR) [6], ISNT [7] and notching, etc. Among them, CDR is well accepted and widely used in real applications. Although these clinical indicators are different from each other, precise information of OD and OC boundary is required for the measurement of such clinical indicators to efficiently assess the glaucoma.

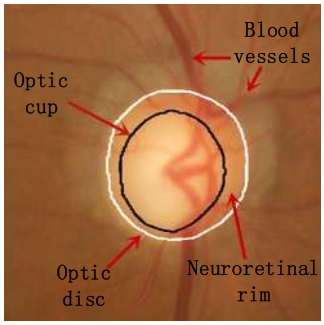

FIGURE 1. Major structures of the optic disc. White line: the optic disc boundary, black line: the optic cup boundary, the region between the white line and black line is the neuroretinal rim.

Many researchers have been put their efforts for automatic segmentation of OD and OC from retinal fundus images. Proposed approaches can mainly be broadly divided into two categories: shape-based and appearance-based. In the shape-based approaches, since the shape of OD and OC is approximately a round or an oval, the edge maps extracted from retinal fundus images are fitted using a circle or ellipse Hough Transform [8]–[10]. However, since the real OD or OC shape is not a regular round or oval, strict fitting cannot satisfy with their original structures. Apart from the aforementioned stiff segmentation methods, a flexible statistical shape model, namely active shape model (ASM) [11]–[13] can represent an OD-OC shape using statistical approaches. Although it can represent the OD-OC shapes accurately, ASM may fail in segmenting that the object with variation and irregularity boundary.

For the appearance-based approaches, they can be further classified into four classes including thresholding [14]–[16], vessel bending [17]–[19], classification-based [5], [20]–[22] and active contour model (ACM) [17], [23], [25], [27], [28]. Considering that the OC is the region of maximum color contrast within the OD, Hatanaka *et al.* [14]–[16] presented some thresholding-based approaches using intensity information for segmenting the boundary of OC. However, there are some problems during identifying the OC region due to intensity inhomogeneity generated by imperfection of image devices or illumination variations as well as obscuration by bridging retinal vessel. To address these issues, W.W.K and Hatanaka [17]–[19] applied the additional information based on vessel kinks to detect OC. However, only a small subset of positions where the vessel bend actually lies on the OC boundary, thereby it is necessary to select several heuristics algorithms to detect vessel kinks. According to Cheng *et al.* [5], [20]–[22], classification-based approaches have also been used to significantly enhance the OD and OC detection. However, it is greatly influenced by sample size (e.g., the small amount of training data will lead to a larger bias for the segmentation results, and it is also time consuming to deal with the large amount of training data). Currently, in view of the complex topological changes of boundary contour and irregular shape caused by peripapillary atrophy (PPA) and vasculature occlusion, some ACM based methods have been developed to evolve the boundary of object during iteration.

Osareh *et al.* [23] located the OD boundary using an automatically initialized snake based on image gradient, which can improve the precision for capturing shape irregularity in the OD area when comparing with the existing approaches. After that, the OD boundary is evolved by a minimization of the effect on the perturbance in the energy value due to the high variations at vessels locations. Inspired by the localized Chan-Vese (CV) models [24], Joshi *et al.* [17] presented a region-based ACM approach to segment OD. Then, the OC boundary is extracted depending on vessel kinks in retinal fundus images. However, this method is only simply added with the equally weighted in local region around each point of interest, it ignores the intrinsic physical meaning and statistical information within the fundus images leading to that the extracted OD boundary is inaccurate. Meanwhile, a majority of blood vessels enter OC from the inferior and superior directions, the estimation of OC boundary always tends to be in nasal and temporal sectors which is easy to be inaccurate. Mittapalli and Kande [25] extended the original local binary fitting (LBF) [26] ACM by incorporating local image information from multiple image channels for segmenting the OD. Then, they combined spatially weighted Fuzzy C-means (SWFCM) clustering and mathematical morphology methods together to extract the OC boundary. Although the methods can achieve OD and OC boundary extraction, there are still three limitations in them. First, since this ACM-based approach employed a hard classification manner for OD boundary extraction, it isn't able to well represent the gradually varying areas that usually exist in retinal images with intensity inhomogeneity, especially for severe intensity inhomogeneity. Second, it neglects the imperfection of the single-view information and can't well deal with the appearance information missing. Third, compared with OD segmentation, the OC segmentation is more challenging. For example, the appearance of OC is always covered by most blood vessels or influenced by uneven illumination leading to that the boundary of OC is obscure or incomplete. Thakur and Juneja [27] presented a hybrid approach named Level Set Adaptively Regularized Kernel-Based Intuitionistic Fuzzy C Means (LARKIFCM) for OD and OC segmentation, which used the level set combined with clustering

approach. It can more effectively segment OD and OC due to taking positive features of the combined approaches. However, this approach ignores the integrated anatomical structure prior information of OD and OC and fails to obtain the accurate boundary of OD and OC in complex retinal image. Gao et al [28] introduced the prior constraint information into Local Image Fitting model which can overcome most of influences caused by bright regions of PPA and achieve a smooth boundary. However, this model leads to inaccurate segmentation in some regions, as the prior information replaces the important intensity information which is insufficient.

Seen from the aforementioned approaches, they extract OD-OC boundaries which are either shape-based or appearance-based approaches. While both of them suffer from the following challenging issues including severe intensity inhomogeneity (see Fig.2(b)), the complex blood vessel structure (see Fig.1) within the retinal images and the PPA (see Fig.2(a)) around the OD. This paper proposes a solution to overcome these issues and presents two novel energy optimization frameworks by fusing the advantages of both types of the approaches. The main contributions are as follows: (1) LSACM is introduced to deal with the severe intensity inhomogeneity which is widely existed in the retinal fundus images. (2) To fully explore the intrinsic structures within the retinal fundus images and make the extracted OD and OC boundaries more integrity, we integrate probability information from a multi-dimensional feature space into our models. (3) Considering that the anatomical structures both of the OD and OC are similar with ellipse shape, the shape priori constraint information is further fused into our models.

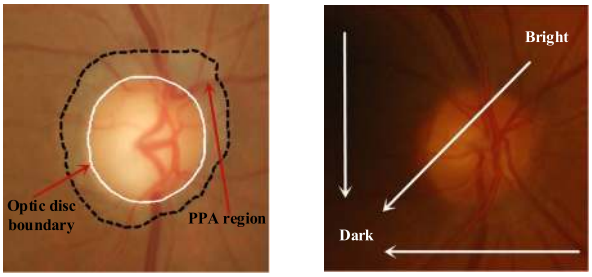

FIGURE 2. Intensity inhomogeneity challenges in optic disc and optic cup segmentation.

II. CONTOUR INITIALIZATION

Based on the cropped ROI around OD as shown in Fig.3(a) which is achieved by our method mentioned in [29], we can further extract the boundaries of the OD and OC. Considering that it is necessary to initialize the presented active contour model, a robust and effective contour initialization method which combines saliency detection and threshold techniques is designed in this subsection.

Because the choroidal vessels are presented in the ROI, it may affect the segmentation accuracy of the OD and OC boundaries. To address this problem, morphological opening followed by closing operations are done on each red, green, and blue channel images to remove the influence of blood vessels and the vessels removal result is shown in Fig.3(b). According to a large number of experimental verifications [2], we choose the disk structure with the radius of 15 pixels as the basic structure element by experience to remove vessels in this paper. Meanwhile, since the OD is usually brighter than other areas in the retinal fundus images, it can be considered as a salient objective. Inspired by saliency detection method to find out the most important region in the image, a cellular (i.e., superpixel) automata based saliency detection method [30], which considers both global color and spatial distance matrices, is applied to contour initialization. First, the cellular automata based saliency detection method [30] is done on the vessels removal image for obtaining the saliency map in which the corresponding output saliency value of each superpixel is continuous between 0 and 1(see Fig.3(c)). Then, in order to obtain smoothed map values, we use the mean filter [5] to process the saliency map (see Fig.3(d)). Considering that the binary decisions for all the pixels need to be obtained by a threshold in the smoothed map (Fig.3(d)), we adopt the Otsu to obtain the threshold and distribute 1 and 0 to OD and non-OD. After that, the object region (OD) is set as 1 and the background region is set as 0. Finally, we can achieve the largest connected object using morphological operation, which is the connected region with the largest number of the pixels (see Fig.3(e)). Its boundary is regarded as the initial contour for segmenting the OD (see Fig.3(f) in green).

The OC is predicted to be either a circular or oval within the OD and is defined as the area of maximum color contrast inside the OD [1], [25]. Compared to the OD, the extraction of the OC boundary is more challenge as it intertwines with the blood vessels or surrounding area. In this paper, the cup boundary is also determined via saliency detection and threshold techniques. The main difference between the OD and the OC contour initialization is the usage of different threshold methods. As the OC is the highest intensity region inside the OD, highest intensity based thresholding approach is suitable for extracting OC initial contour. First, thresholding [31] is empirically applied on the smoothed map image (Fig.3(d)) with the value of threshold 10% of the highest intensity value and the obtained binary image is shown in Fig.3(g). Then, Hough transform is done on the estimated cup boundary (Fig.3(h)) which helps to obtain an overall boundary of the identified cup region as well as smoothing the region boundary. The result of the Hough transform is used as the OC initialization contour, as shown in Fig.3(i)(blue).

III. THE PROPOSED METHODS

A. LOCALLY STATISTICAL ACTIVE CONTOUR MODEL (LSACM)

The changes of OD and OC will indicate the severity of glaucoma illness. The precision of boundary extraction of OD and OC is necessary to study the process of glaucoma illness and treatment results. However, intensity inhomogeneity phenomenon widely exists in retinal image caused

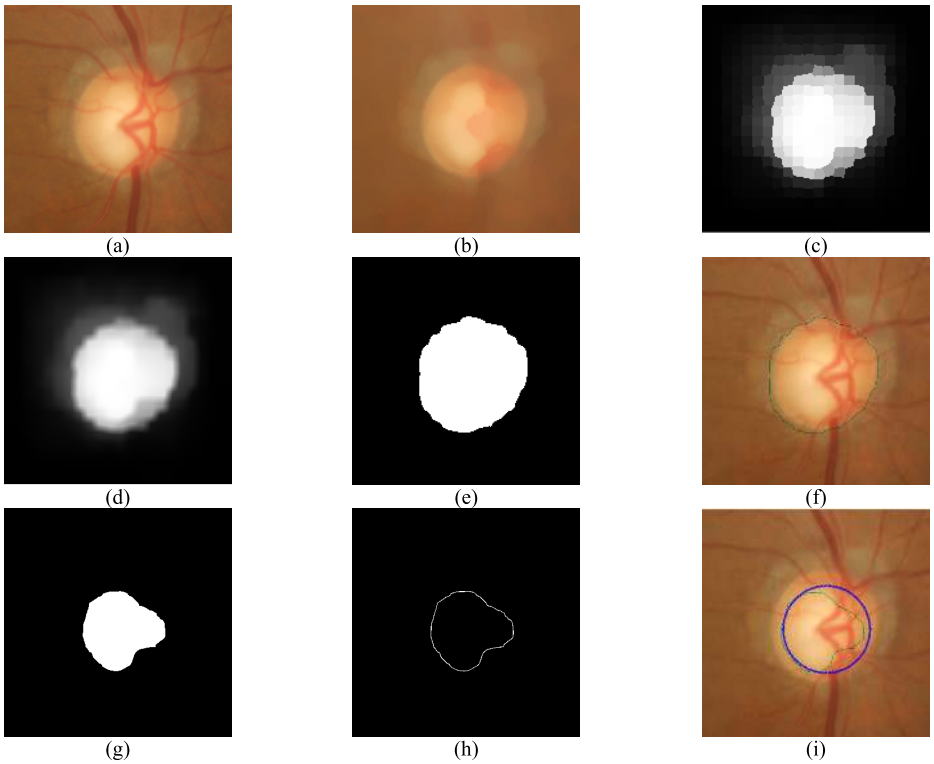

FIGURE 3. Contour initialization. (a) cropped ROI around optic disc, (b) vessels removal, (c) saliency detection result, (d) smoothed image of (c), (e) the largest connected object, (f) optic disc initial contour (green), (g) the binary image of (d) using thresholding, (h) the edge image of (g), (i) the obtained cup initial contour after Hough transform (blue).

by imperfection of image devices or illumination variations seriously influencing OD and OC segmentation. In order to deal with the problem, in this paper, we introduce the Locally Statistical Active Contour Model (LSACM) [32] to model the inhomogeneous objects as Gaussian distributions of different means and variances. In LSACM, a sliding window is used to map the original image into another domain, where the intensity distribution of each object with intensity inhomogeneity has less overlapping in the statistics. Besides a maximum likelihood energy functional is solved to approximate the true image signal. More detailed descriptions can refer to [32].

For a given input image I, the LSACM model [32] defines an energy functional as

$$E_{LSACM} = \sum_{j=1}^{n} \int_{\Omega} F_j(y) M_j(\Phi(y)) dy \tag{1}$$

where

$$F_j(y) \triangleq \int_{\Omega} K_\rho(x,y) \left(\log(\sigma_j) + \left((I(y) - B(x) c_j)^2 \Big/ 2\sigma_j^2\right)\right) dx$$

$$K_\rho(x,y) = \begin{cases} 1, & |y-x| \le \rho \\ 0, & else. \end{cases}$$

$$M_j(\Phi(y)) = \begin{cases} 1, & y \in \Omega_j \\ 0, & else. \end{cases}$$

where the symbol $\Re$ represents the set of real number, pixel coordinates $x, y \in \Omega \subset \Re^2$, $\Omega = \cup_{j=1,\ldots,n}\Omega_j$ is image domain where Ω_j can be expressed as the domain of the j-th object and $\Omega_j \cap \Omega_i = \Theta$ for all $j \neq i$. Θ is an empty set. n represent the total number of objects in image I. $I(y)$ denotes the pixel value at the pixel coordinate y. The symbol O_x denotes a neighboring region centering at location x, i.e., $O_x = \{y \,||y-x| \le \rho\}$, y is the neighborhood point relative to x and ρ is the radius of the region O_x. c_j is assumed to be the true signal of the j-th object which is always considered as a piecewise constant within object domain. $B(x)$ is the bias field function. $B(x) c_j$ is the spatial varying mean that is estimated at the local region $\Omega_j \cap O_x$ centered at each location x, σ_j is the standard deviation of the Gaussian distribution for the j-th object. $M_j(\Phi(y))$ is the membership function of the region Ω_j and $M_j(\Phi(y)) = 1$ when $y \in \Omega_j$, otherwise $M_j(\Phi(y)) = 0$. $\Phi(y)$ is the set of level set functions. $K_\rho(x,y)$ is the indicator function of a local region O_x.

B. THE SEGMENTATION OF OPTIC DISC

Apart from intensity inhomogeneity, other conditions, such as boundary smoothing, blood vessels covering and image variations near the OD boundary due to pathological changes, make the segmentation of the OD more challenging. To overcome the above problems, we extract multi-view information

based on the appearance and shape of OD aiming to achieve accurate OD detection in varied conditions.

1) COMBINING LSACM WITH THE INFORMATION OF APPEARANCE (LSACM-A)

Based on the appearance of OD, the LSACM is extended by integrating the local image probability information around the point of interest from a multi-dimensional feature space.

According to the [32], The Gaussian Probability Density Function (PDF) based on the transformed domain for the j-th object at the pixel x in a single feature space can be described as follows:

$$P(I'(x/\theta_j, B)) \propto \prod_{y\in\Omega_j\cap O_x} P(I(y|\theta_j, B, x)) \tag{2}$$

where

$$P(I(y|\theta_j, B, x)) = \frac{1}{\sqrt{2\pi}\sigma_j}\exp(-\frac{(I(y) - B\,(x)\,c_j)^2}{2\sigma_j^2})$$

where I' is the image in the transformed domain. $P(I(y|\theta_j, B, x))$ is the Gaussian PDF for the j-th object at the pixel y near the pixel x in a single feature space. Π is denoted as multiplication. θ_j denotes the set of estimated parameters $\{c_j, \sigma_j\}$.

Now, we integrate probability information from a multi-dimensional feature space and the working mechanism is depicted in the Fig.4 Based on the mentioned Gaussian PDF for the transformed domain, the proposed probability function based on the transformed domain for the j-th object at the pixel x is depicted in Eq. (3). It combines a richer form of the local image probability information at the point of interest gathered over a multi-dimensional feature space.

$$\prod_{i=1}^{d} P_i(I_i'(x/\theta_{ji}, B_i)) \propto \prod_{i=1}^{d}\prod_{y\in\Omega_j\cap O_x} P_i(I_i(y|\theta_{ji}, B_i, x)) \tag{3}$$

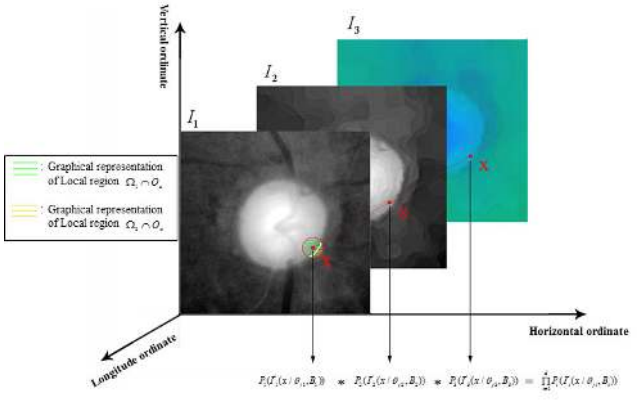

FIGURE 4. Scheme illustration of joint probability information from a multi-dimensional feature space. A set of feature images constitute a multi-dimensional feature space. All of the Gaussian PDFs based on the transformed domain for the j-th object at the pixel x in different dimensional feature spaces multiply (e.g. $j = 1, 2; i = 1, 2, 3$).

where

$$P_i(I_i(y|\theta_{ji}, B_i, x)) = \frac{1}{\sqrt{2\pi}\sigma_{ji}}\exp(-\frac{(I_i(y) - B_i\,(x)\,c_{ji})^2}{2\sigma_{ji}^2})$$

where $P_i(I_i'(x/\theta_{ji}, B_i))$ is the Gaussian PDF based on the transformed domain for the j-th object at the pixel x in the i-th feature space. $P_i(I_i(y|\theta_{ji}, B_i, x))$ is the Gaussian PDF for the j-th object at the pixel y near the pixel x in the i-th feature space. d is denoted as the sum of feature spaces. I_i is the input image in the i-th feature space. I_i' is the image in the transformed domain for the i-th feature space. θ_{ji} is the set of estimated parameters $\{c_{ji}, \sigma_{ji}\}$. B_i is the bias field function in i-th feature space. $B_i(x)c_{ji}$ is the spatial varying mean that is estimated at the local region $\Omega_j\cap O_x$ centered at each location x in the i-th feature space. c_{ji} is assumed to be the true signal of the j-th object in the i-th feature space. σ_{ji} is the standard deviation of the Gaussian distribution for the j-th object in the i-th feature space.

Supposing that $D = \{I'(x/\theta_{ji}, B_i), x \in \Omega, j = 1, \ldots, n; i = 1, \ldots, d\}$, based on the proposed probability function by combining multi-dimensional features probability information, the joint likelihood function can be described as follows [32]:

$$\begin{aligned} P(D/\theta, B) &= \prod_{j=1}^{n}\prod_{x\in\Omega}\prod_{i=1}^{d} P_i(I_i'(x/\theta_{ji}, B_i)) \\ &\propto \prod_{j=1}^{n}\prod_{x\in\Omega}\prod_{i=1}^{d}\prod_{y\in\Omega_j\cap O_x} P_i(I_i(y|\theta_{ji}, B_i, x)) \end{aligned} \tag{4}$$

where $\theta = \{\theta_{ji}, j = 1, \ldots, n; i = 1, \ldots, d\}$, $B = \{B_i, i = 1, \ldots, d\}$, n describes the sum of objects.

Similar to the [32], in order to evaluate the parameter set $\tilde{\theta}$ and $\tilde{B}$, the inverse log-likelihood function of $P(D/\theta, B)$ is defined. Meanwhile, we also eliminate the trivial constant term and add the constant weight coefficient. The novel model based on the appearance can be obtained as follows:

$$E_{LSACM-A} = \frac{1}{d}\sum_{i=1}^{d}\sum_{j=1}^{n}\int_{\Omega} F_{ji}(y)M_j(\phi(y))dy \tag{5}$$

where

$$F_{ji}(y) \triangleq \int_{\Omega} K_\rho(x, y)(\log(\sigma_{ji}) + ((I_i(y) - B_i(x)c_{ji})^2/2\sigma_{ji}^2))dx$$

$$M_1 = H(\phi(y)); \quad M_2 = 1 - H(\phi(y))$$

Because the OD is brighter than other areas in the retinal fundus images [33], we set number of objects n as 2; $c_{1i} = (c_{11}, c_{12}, \ldots, c_{1d})$, $c_{2i} = (c_{21}, c_{22}, \ldots, c_{2d})$, $B_i = (B_1, B_2, \ldots, B_d)$, $\sigma_{1i} = (\sigma_{11}, \sigma_{12}, \ldots, \sigma_{1d})$ and $\sigma_{2i} = (\sigma_{21}, \sigma_{22}, \ldots, \sigma_{2d})$ are five constant vectors. The values of the two vectors c_{1i} and c_{2i} respectively are assumed to be the true signal of the OD and the background in i-th feature space. The values of the two vectors σ_{1i} and σ_{2i} respectively express standard deviation of the Gaussian distribution of the OD and the background in i-th feature space. H represents the

Heaviside function. ϕ is the level set function for segmenting the OD. The values of c_{1i}, c_{2i}, B_i, σ_{1i} and σ_{2i} are optimally chosen by minimizing the above energy function (5).

Due to the complex OD appearance (e.g. illumination variations, the anomalies influence and intertwined blood vessels), the complete OD can't be well described by single-feature space. So, the multi-feature spaces need to be integrated to complement each other's advantages for adequately describing the OD. Considering that the red color plane has an unobvious contrast for blood vessel and gives a better contrast of the OD region [17], and the HSV color space can easily separate the intensity information from the color information and retrieve more information [34]. Then, the extended LSACM uses a multi-dimensional feature space ($d = 5$) where the individual vector element is taken from red color plane, vessel-free red color plane, and each channel from vessel-free HSV color space, to represent an image point x. Finally, the extracted OD boundary is shown in Fig.5(b).

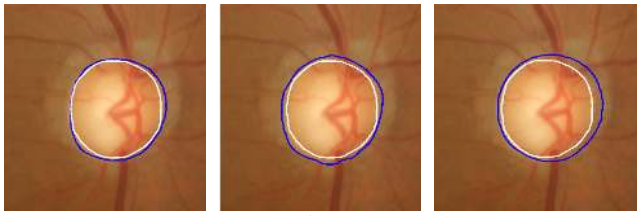

(a) (b) (c)

FIGURE 5. The extracted OD boundaries. (a) The result obtained by LSACM-AS, (b) the result obtained by LSACM-A, (c) the result obtained by LSACM-S.

2) COMBINING LSACM WITH THE INFORMATION OF SHAPE (LSACM-S)

Considering that the shape of OD is a circular or elliptic region [29], [35], [36], the shape priori information of the OD is introduced into the LSACM maintaining the intrinsic anatomical structure.

First, the elliptic parameterized level set function of the OD which consists of a five-tuple $(x_d, y_d, \theta_d, a_d, b_d)$ is introduced. It can be described as:

$$\phi_o = 1 - \sqrt{\frac{A^2}{a_d^2} + \frac{B^2}{b_d^2}} \tag{6}$$

where

$$A = (x - x_d)\cos\theta_d + (y - y_d)\sin\theta_d$$
$$B = -(x - x_d)\sin\theta_d + (y - y_d)\cos\theta_d$$

where x_d and y_d are oval center coordinates, a_d is defined as the scaling factor of semi-major axis length and b_d is the semi-minor axis length, θ_d is the angle of rotation.

Then, we construct an ellipse constraint term based on the elliptic parameterized level set function ϕ_o for the OD. It can be shown as follows:

$$E_{ShapePrior} = \int_{\Omega} \nu(H(\phi(y)) - H(\phi_o(y)))^2 dy \tag{7}$$

where

$$\phi_o = 1 - \sqrt{\frac{A^2}{a_d^2} + \frac{B^2}{b_d^2}}$$

where

$$A = (x - x_d)\cos\theta_d + (y - y_d)\sin\theta_d$$
$$B = -(x - x_d)\sin\theta_d + (y - y_d)\cos\theta_d$$

where ν is the constraint coefficients for ellipse to determine the weight of elliptic constraint. The term (7) simultaneously drives ϕ and ϕ_o, and it is symmetric to ϕ and ϕ_o to constrain the zero level set of ϕ as an ellipse.

The extended LSACM by integrating the ellipse constraint term can be expressed as:

$$E = \sum_{j=1}^{n} \int_{\Omega} F_j(y) M_j(\phi(y)) dy + \int_{\Omega} \nu(H(\phi(y)) - H(\phi_o(y)))^2 dy \tag{8}$$

where

$$F_j(y) \triangleq \int_{\Omega} K_\rho(x, y) \left(\log(\sigma_j) + \left((I(y) - B(x) c_j)^2 \Big/ 2\sigma_j^2 \right) \right) dx$$
$$M_1 = H(\phi(y)); \quad M_2 = 1 - H(\phi(y))$$

where the number of objects n is also set as 2 as in the previous section. Both of them constantly change with the curve evolution.

Besides, in order to extract a smoother contour without drastic protuberance and sunken, the penalizing length item is used to regularize the zero level contour of the level set function ϕ. It can be integrated with formula (8) and the entire energy functional can be defined as:

$$E_{LSACM-S} = \sum_{j=1}^{n} \int_{\Omega} F_j(y) M_j dy + \int_{\Omega} \lambda |\nabla H(\phi(y))| dy + \int_{\Omega} \nu(H(\phi(y)) - H(\phi_o(y)))^2 dy \tag{9}$$

where λ is the weight length of zero level curve of ϕ.

We can see that integrating the LSACM with the shape prior information together can both extract the boundary of the OD and maintain the intrinsic ellipse structure as shown in Fig.5(c).

Considering the above appearance and shape information for OD, in order to fully explore the structure of OD and extract the robust OD boundary, we combine the multi-view information by fusing both the appearance and shape of the OD with LSACM (LSACM-AS) and propose the following objective function $E_{LSACM-AS}$:

$$E_{LSACM-AS} = \frac{1}{d} \sum_{i=1}^{d} \sum_{j=1}^{n} \int_{\Omega} F_{ji}(y) M_j dy + \int_{\Omega} \lambda |\nabla H(\phi(y))| dy + \int_{\Omega} \nu(H(\phi(y)) - H(\phi_o(y)))^2 dy \tag{10}$$

3) ENERGY MINIMIZATION PROCESS FOR LSACM-AS

We use the standard gradient descent method [32] to minimize the proposed energy functional in Eq. (10). Seen from (10), it is a hard work to find a minimizer $E_{LSACM-AS}$ for ϕ, c_{1i}, c_{2i}, B_i, σ_{1i}, σ_{2i}, x_d, y_d, θ_d, a_d and b_d simultaneously. Consequently, we solve the minimization problem for each variable alternatively to find a minimizer of (10).

For a fixed $\phi, x_d, y_d, \theta_d, a_d, b_d$, functional Eq. (10) is minimized with respect to the $c_{1i}, c_{2i}, B_i, \sigma_{1i}, \sigma_{2i}$ $(i = 1, 2, \ldots, d)$ as:

$$c_{1i} = \frac{\int_{\Omega} [K_\rho(x,y) \otimes B_i(x)] I_i(y) H(\phi(y)) dy}{\int_{\Omega} [K_\rho(x,y) \otimes B_i^2(x)] H(\phi(y)) dy} \tag{11}$$

$$c_{2i} = \frac{\int_{\Omega} [K_\rho(x,y) \otimes B_i(x)] I_i(y) (1 - H(\phi(y))) dy}{\int_{\Omega} [K_\rho(x,y) \otimes B_i^2(x)] (1 - H(\phi(y))) dy}$$

$$B_i(x) = \frac{K_\rho(x,y) \otimes [I_i(y) H(\phi(y))] \frac{c_{1i}}{\sigma_{1i}^2}}{K_\rho(x,y) \otimes [H(\phi(y))] \frac{c_{1i}^2}{\sigma_{1i}^2}} + \frac{+K_\rho(x,y) \otimes [(1 - H(\phi(y)))] \frac{c_{2i}^2}{\sigma_{2i}^2}}{K_\rho(x,y) \otimes [H(\phi(y))] \frac{c_{1i}^2}{\sigma_{1i}^2}} + K_\rho(x,y) \otimes [I_i(y)(1 - H(\phi(y)))] \frac{c_{2i}}{\sigma_{2i}^2} \tag{13}$$

$$\sigma_{1i} = \sqrt{\frac{\int_{\Omega}\int_{\Omega} K_\rho(x,y)(I_i(y) - B_i(x)c_{1i})^2 H(\phi(y)) dxdy}{\int_{\Omega}\int_{\Omega} K_\rho(x,y) H(\phi(y)) dxdy}} \tag{14}$$

$$\sigma_{2i} = \sqrt{\frac{\int_{\Omega}\int_{\Omega} K_\rho(x,y)(I_i(y) - B_i(x)c_{2i})^2 (1 - H(\phi(y))) dxdy}{\int_{\Omega}\int_{\Omega} K_\rho(x,y)(1 - H(\phi(y))) dxdy}} \tag{15}$$

Keeping ϕ, c_{1i}, c_{2i}, B_i, σ_{1i}, σ_{2i} fixed, minimizing the energy functional Eq.(10) with respect to x_d, y_d, θ_d, a_d, b_d, some gradient vector flows are obtained:

$$\frac{dx_d}{dt} = 2v \int_{\Omega} L\left(\frac{A\cos\theta_d}{a_d^2} + \frac{-B\sin\theta_d}{b_d^2}\right) dy \tag{16}$$

$$\frac{dy_d}{dt} = 2v \int_{\Omega} L\left(\frac{A\sin\theta_d}{a_d^2} + \frac{B\cos\theta_d}{b_d^2}\right) dy \tag{17}$$

$$\frac{d\theta_d}{dt} = 2v \int_{\Omega} L\left(\frac{-AB}{a_d^2} + \frac{AB}{b_d^2}\right) dy \tag{18}$$

$$\frac{da_d}{dt} = 2v \int_{\Omega} L\left(\frac{A^2}{a_d^3}\right) dy \tag{19}$$

$$\frac{db_d}{dt} = 2v \int_{\Omega} L\left(\frac{B^2}{b_d^3}\right) dy \tag{20}$$

where

$$L = (H(\phi) - H(\phi_o))\delta(\phi_o) \times \left(\frac{A^2}{a_d^2} + \frac{B^2}{b_d^2}\right)^{-\frac{1}{2}}$$

Keeping c_{1i}, c_{2i}, B_i, σ_{1i}, σ_{2i}, x_d, y_d, θ_d, a_d, b_d fixed and minimizing the energy functional Eq.(10) with respect to ϕ, we obtain the gradient vector flow as:

$$\frac{\partial\phi}{\partial t} = \lambda div\left(\frac{\nabla\phi}{\sqrt{\phi_x^2 + \phi_y^2}}\right)\delta(\phi) - \frac{1}{d}\sum_{i=1}^{d}(F_{1i} - F_{2i})\delta(\phi) - 2v(H(\phi) - H(\phi_o))\delta(\phi) \tag{21}$$

4) REGULARIZE LEVEL SET FUNCTION

In order to keep numerical implementation stable, we need to regularize the level set function during the iteration [32]. In the paper, a simple and stable approach is used [32] to regularize the level set function which is completely free of the costly reinitialization procedure in the level set evolution. The level set function is regularized by the Eq. (22):

$$\phi^{l+1} = \phi^l + \Delta t \cdot \nabla^2 \phi^l \tag{22}$$

where ϕ^l is the evolved level set function for OD obtained from the l-th iteration, Δt is the time steps, ∇^2 denotes the Laplacian operator. The object function (10) is minimized by solving Eq. (11) $\sim$ (22).

5) DIFFERENT SEGMENTATION RESULTS ACHIEVED BY METHODS INTEGRATING INFORMATION OF APPEARANCE AND SHAPE

Seen from Fig.5(a), in terms of the appearance information integrated from a multi-dimensional feature space including the vessel-free information and the unabridged information for the OD, it can be used to cooperate with the contour evolving into ideal similar ellipse due to the function of ellipse constraint item. This process can not only recover the missing parts of appearance information, but also remove the occlusion parts of appearance information. Hence, the evolution contour obtained by LSACM-AS is robust to the situations of the boundary smoothing, the influence of blood vessels and pathological changes. The boundary of OD extracted by LSACM-AS is more precise than other methods, such as only combining the information of appearance (see Fig.5(b)) or shape (see Fig.5(c)).

C. THE SEGMENTATION OF OPTIC CUP

The OC shape is predicted to be either circular or oval shape, which is appeared as the area of maximum color contrast inside the OD [1], [25]. Compared with OD segmentation, the OC segmentation is more challenging since the dense blood vessels cover parts of the cup leading to the gradual change in color intensity between the rim and cup. In this paper, we use the same manner likes OD segmentation which is based on multi-view information about the appearance and shape of OD to segment OC. However, the proposed approach for segmenting the OD can't be directly applied

for segmenting the OC. The main reason is that both the OD and the OC is a complete bright region (optic nerve head) compared to the background, and thereby two-phase LSACM using one level set to represent two objects and four-phase LSACM using two level set to represent four objects can't directly extract the boundary of the OC due to the special structure relationship. To address this issue, we design a novel preprocessing approach which introduces a structure prior information constraint into the contour evolution to achieve OC segmentation. In this paper, the preprocessing is mainly to constrain the effective evolution range, i.e., the evolution of the OC should be done inside the OD region which is expressed as the region that is the level set function ϕ greater than zero ($\phi > 0$). The modified LSACM (MLSACM) by our preprocessing method is defined as follows:

$$E_{MLSACM} = \sum_{j=3}^{p} \int_{\Omega} f_j(y)\, M_j(\varphi(y))dy \tag{23}$$

where

$$f_j(y) \triangleq \int_{\Omega} K_\rho(x,y)\left(\log(\sigma_j) + \left((I(y) - b(x)\,c_j)^2 \Big/ 2\sigma_j^2\right)\right)dx$$
$$M_3 = H(\phi(y))H(\varphi(y)); \quad M_4 = H(\phi(y))(1 - H(\varphi(y)))$$

where we set p as 4. $j = 3$ and $j = 4$ respectively denote two different regions in OD including the OC and the neuroretinal rim. b is the bias field function for calculating the OC. ϕ is the level set function for the OD, φ is the level set function for the OC. M_3 and M_4 are proposed to represent the intrinsic anatomical structure of the OC. Namely, both of them are the membership functions for inner and outer regions of the OC in the OD region extracted by the proposed OD segmentation method.

Similar to the segmentation of OD, the MLSACM blended in multi-view information about the appearance and shape of the OC for extracting the OC boundary is defined as:

$$E_{MLSACM-AS} = \frac{1}{m}\sum_{i=1}^{m}\sum_{j=3}^{p}\int_{\Omega} f_{ji}(y)M_j dy + \int_{\Omega}\mu|\nabla H(\varphi(y))|dy + \int_{\Omega}\gamma(H(\varphi(y)) - H(\varphi_o(y)))^2 dy \tag{24}$$

where

$$f_{ji}(y) \triangleq \int_{\Omega} K_\rho(x,y)(\log(\sigma_{ji}) + ((I_i(y) - b_i(x)c_{ji})^2/2\sigma_{ji}^2))dx$$
$$M_3 = H(\phi(y))H(\varphi(y)); \quad M_4 = H(\phi(y))(1 - H(\varphi(y)))$$
$$\varphi_o = 1 - \sqrt{\frac{C^2}{a_c^2} + \frac{D^2}{b_c^2}}$$

where

$$C = (x - x_c)\cos\theta_c + (y - y_c)\sin\theta_c$$
$$D = -(x - x_c)\sin\theta_c + (y - y_c)\cos\theta_c$$

where $c_{3i} = (c_{31}, c_{32}, \ldots, c_{3m})$, $c_{4i} = (c_{41}, c_{42}, \ldots, c_{4m})$, $b_i = (b_1, b_2, \ldots, b_m)$, $\sigma_{3i} = (\sigma_{31}, \sigma_{32}, \ldots, \sigma_{3m})$ and $\sigma_{4i} = (\sigma_{41}, \sigma_{42}, \ldots, \sigma_{4m})$ are five constant vectors. m is denoted as the sum of feature spaces for the OC segmentation. The values of the two vectors c_{3i} and c_{4i} respectively are assumed to be the true signal of the OC and neuroretinal rim in i-th feature space. The value of vector b_i is the bias field function for calculating OC in i-th feature space. $b_i(x)c_{ji}$ is the spatial varying mean that is estimated at the local region $\Omega_j \cap O_x$ centered at each location x in i-th feature space. The values of the two vectors σ_{3i} and σ_{4i} respectively express standard deviation of the Gaussian distribution of the OC and the neuroretinal rim in i-th feature space. The values of c_{3i}, c_{4i}, b_i, σ_{3i} and σ_{4i} are optimally chosen such that the above energy function (24) is minimized when the evolution contour is near the true OC boundary. φ_o is the elliptic parameterized level set function of the OC, x_c and y_c are oval center coordinates, a_c is a scaling factor of semi-major axis length, b_c is a scaling factor of semi-minor axis length, θ_c is the angle of rotation. Both of them constantly change with the level set function φ evolving. γ is a constraint coefficient for ellipse which determines the weight of elliptic constraint, μ is the weight length of zero level curve of φ. In this subsection, due to the complex OC appearance (e.g. illumination variations, intertwined blood vessels), the complete OC can't be well described by single-feature space. So, the multi-feature spaces need to be integrated to complement each other's advantages for adequately describing the OC. Considering that the intensity information from the color information can be easily separated and more information can be retrieved in the HSV color space [34], and the green color plane provides a better contrast for OC [37]. Then, we use a multi-dimensional feature space ($m = 5$) which consists of red color plane, vessel-free green color plane and each channel from vessel-free HSV color space to describe an image point x.

The boundary of OC can be extracted by using the standard gradient descent approach to minimize the proposed energy functional in Eq. (24). Some minimizers and some gradient vector flows are given as follows:

$$c_{3i} = \frac{\int_{\Omega}[K_\rho(x,y)\otimes b_i(x)]I_i(y)H(\phi(y))H(\varphi(y))dy}{\int_{\Omega}[K_\rho(x,y)\otimes b_i^2(x)]H(\phi(y))H(\varphi(y))dy} \tag{25}$$

$$c_{4i} = \frac{\int_{\Omega}[K_\rho(x,y)\otimes b_i(x)]I_i(y)H(\phi(y))(1 - H(\varphi(y)))dy}{\int_{\Omega}[K_\rho(x,y)\otimes b_i^2(x)]H(\phi(y))(1 - H(\varphi(y)))dy}$$

$$b_i(x) = \frac{\times K_\rho(x,y)\otimes[I_i(y)H(\phi(y))H(\varphi(y))]\frac{c_{3i}}{\sigma_{3i}^2} + K_\rho(x,y)\otimes[I_i(y)H(\phi(y))(1 - H(\varphi(y)))]\frac{c_{4i}}{\sigma_{4i}^2}}{K_\rho(x,y)\otimes[H(\phi(y))H(\varphi(y))]\frac{c_{3i}^2}{\sigma_{3i}^2} + K_\rho(x,y)\otimes[H(\phi(y))(1 - H(\varphi(y)))]\frac{c_{4i}^2}{\sigma_{4i}^2}} \tag{26, 27}$$

$$\sigma_{3i} = \sqrt{\frac{\int\int_{\Omega\,\Omega} K_\rho(x,y)(I_i(y)-b_i(x)c_{3i})^2 H(\phi(y))H(\varphi(y))dxdy}{\int\int_{\Omega\,\Omega} K_\rho(x,y)H(\phi(y))H(\varphi(y))dxdy}} \tag{28}$$

$$\sigma_{4i} = \sqrt{\frac{\int\int_{\Omega\,\Omega} K_\rho(x,y)(I_i(y)-b_i(x)c_{4i})^2 H(\phi(y))(1-H(\varphi(y)))dxdy}{\int\int_{\Omega\,\Omega} K_\rho(x,y)H(\phi(y))(1-H(\varphi(y)))dxdy}} \tag{29}$$

$$\frac{dx_c}{dt} = 2\gamma \int_\Omega Z\left(\frac{C\cos\theta_c}{a_c^2} + \frac{-D\sin\theta_c}{b_c^2}\right)dy \tag{30}$$

$$\frac{dy_c}{dt} = 2\gamma \int_\Omega Z\left(\frac{C\sin\theta_c}{a_c^2} + \frac{D\cos\theta_c}{b_c^2}\right)dy \tag{31}$$

$$\frac{d\theta_c}{dt} = 2\gamma \int_\Omega Z\left(\frac{-CD}{a_c^2} + \frac{CD}{b_c^2}\right)dy \tag{32}$$

$$\frac{da_c}{dt} = 2\gamma \int_\Omega Z\left(\frac{C^2}{a_c^3}\right)dy \tag{33}$$

$$\frac{db_c}{dt} = 2\gamma \int_\Omega Z\left(\frac{D^2}{b_c^3}\right)dy \tag{34}$$

where

$$\begin{aligned} Z &= (H(\varphi) - H(\varphi_o))\delta(\varphi_o) \times \left(\frac{C^2}{a_c^2} + \frac{D^2}{b_c^2}\right)^{-\frac{1}{2}} \\ \frac{\partial\varphi}{\partial t} &= \mu div\left(\frac{\nabla\varphi}{\sqrt{\varphi_x^2+\varphi_y^2}}\right)\delta(\varphi) - \frac{1}{m}\sum_{i=1}^{m}(f_{3i}-f_{4i})H(\phi)\delta(\varphi) \\ &\quad - 2\gamma(H(\varphi) - H(\varphi_o))\delta(\varphi) \end{aligned} \tag{35}$$

We also regularize the level set function φ using the same method likes the OD level set function evolution. The level set function φ is regularized by the Eq. (36) after each iteration of (35)

$$\varphi^{l+1} = \varphi^l + \Delta t \cdot \nabla^2\varphi^l \tag{36}$$

where φ^l is the evolution level set function for OC obtained from the l-th iteration. The OC boundary can be extracted by minimizing the objective function in (24).

The final OC boundary extraction results obtained by three methods are shown in Fig.6. They are respectively the modified LSACM with appearance (MLSACM-A), modified LSACM with shape (MLSACM-S) and modified LSACM with both of appearance and shape (MLSACM-AS). Seen from Fig.6, the MLSACM-AS can achieve a satisfied result (Fig.6(a)) compared with MLSACM-A (Fig.6(b)) and MLSACM-S (Fig.6(c)). The main reason lies in the fact that the sufficient appearance information, which include the vessel-free information and the unabridged information for the OC, can be used to cooperate with the contour evolving into ideal similar ellipse due to the function of ellipse constraint item. This process can not only recover the missing parts of appearance information of the OC but also remove the occlusion parts of appearance information caused by blood vessel. Therefore, our approach is robust to the varying structure of OC.

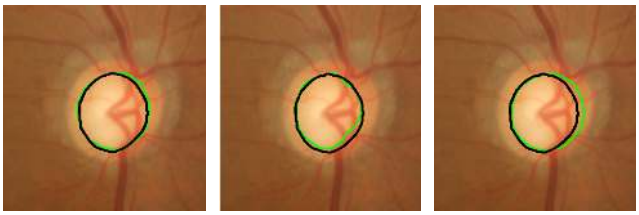

(a) (b) (c)

FIGURE 6. The extracted OC results. (a) The result obtained by MLSACM-AS, (b) the result obtained by MLSACM-A, (c) the result obtained by MLSACM-S.

IV. SIMULATION RESULTS

A. DATABASE

In this paper, the proposed methods for segmenting the OD and the OC were tested on the public dataset of retinal images namely DRISHTI-GS [38]. The dataset totally has 101 images consisting of 31 normal images and 70 glaucomatous images. These images are generated with 30^0 degree field of view and have a resolution of 2896×1944. For each image, the OD and the OC are correctly marked by four glaucoma experts. To compensate for inter-observer marking variations, we acquire a majority voting manual marking as the final ground truth which indicates agreement among at least three experts [38] to qualitatively assess the presented methods.

B. IMPLEMENTATION

In the test, first, the evolution contour computed by all methods for segmenting the OD and the OC uses the initial contours depicted in Section 2. Some parameters for computing the objective function are empirically set such as $\rho = 6$, $\nu = 1.0$, $\gamma = 1.0$ and time step $V_t = 0.45$. All of contrastive segmentation methods are calculated in the vessel-free image. The final segmentation results for the OD and the OC obtaining by optimizing the proposed objective functions are respectively shown in Fig.7(c) and Fig 8(c), in which the Fig.7(a) and the Fig.8(a) depicts the original image. The marked ground truths are respectively shown in Fig.7(b) and Fig.8(b).

C. EVALUATION MEASUREMENTS

The proposed OD segmentation method will be compared with five commonly segmented approaches for the OD, namely C-V model [16], Local Clustering Criterion (LIC) model [39], modified Local Binary Fitting (LBF) [25], LARKIFCM [27], Local Image Fitting model with oval-shaped constraint (LIFO) [28]. Similarly, using four different methods including thresholding [16], ellipse fitting [40], clus-

Algorithm 1 Segmentation for the OD and the OC

LSACM-AS SEGMENTATION STEP:

1. Initialization: Input the set of multi-channel images including original red channel image, vessel-free red channel image, vessel-free green channel image and each channel from vessel-free HSV color space, $i = 1, 2, 3, 4, 5$, $B_i(x) = b_i(x) = 1$, $\sigma_{ji} = j$ (j is taken as both variable value and index), $j = 1, 2, 3, 4$, $x_d = wide/2$, $x_c = wide/2$, $y_d = height/2$, $y_c = height/2$, $\theta_d = \theta_c = 0$, $a_d = (\sqrt{wide^2 + height^2})/8$, $a_c = (\sqrt{wide^2 + height^2})/13$, $b_d = (\sqrt{wide^2 + height^2})/8$, $b_c = (\sqrt{wide^2 + height^2})/13$, the level set functions $\phi^l = \phi^0$, $\varphi^l = \varphi^0$, $\phi_o^l = \phi_o^0$, $\varphi_o^l = \varphi_o^0$, r, l, t, q denotes iterations.
2. Respectively update c_{ji}, B_i, σ_{ji}, $j = 1, 2$, $i = 1, 2, 3, 4, 5$,using (11) $\sim$ (15).
3. The five-tuple (x_d, y_d, θ_d, a_d, b_d) for the elliptical parameterized level set function of the OD is evolved by standard gradient descent method according to (16) $\sim$ (20), if x_d^r, y_d^r, θ_d^r, a_d^r, b_d^r satisfy the stationary condition, then stop; else $r = r+1$ and return to Step 3.
4. Evolve the level set functions, according to (21), regularize the level set functions, using (22). If ϕ^l satisfy the stationary condition, stop; otherwise, $l = l + 1$ and return to Step 2.

MLSACM-AS SEGMENTATION STEP:

5. Input level set function ϕ of the OD obtaining in Step 4.
6. Respectively update c_{ji}, b_i, $\sigma_{ji} j = 3, 4$, $i = 1, 2, 3, 4, 5$, using (25) $\sim$ (29).
7. The five-tuple (x_c, y_c, θ_c, a_c, b_c) for the elliptical parameterized level set function of the OC is evolved by standard gradient descent method according to (30) $\sim$ (34), if x_c^t, y_c^t, θ_c^t, a_c^t, b_c^t satisfy the stationary condition, stop; otherwise, $t = t + 1$ and return to Step 7.
8. Evolve the level set functions, according to (35), regularize the level set functions, using (36). If φ^q satisfy the stationary condition, stop; otherwise, $q = q+1$ and return to Step 6.

tering [25] and LARKIFCM [27] produce an obvious contrast to the proposed approach for the OC.

In order to evaluate the overall performance of both the OD and the OC segmentation approaches, the common quantitative analysis methods are used including detected area, boundary localization and CDR estimation.

First, the detected area assessment is based on the area overlap between the obtained segmentation region and the ground truth marked by the expert. Furthermore, to assess the detected area, the pixel-wise precision and recall values are required to be computed and defined as:

$$precision = \frac{TP}{TP + FP}; \quad recall = \frac{TP}{TP + FN}$$

where TP is the value of true positive, FP is the value of false positive, and FN is the value of false negative. The calculation

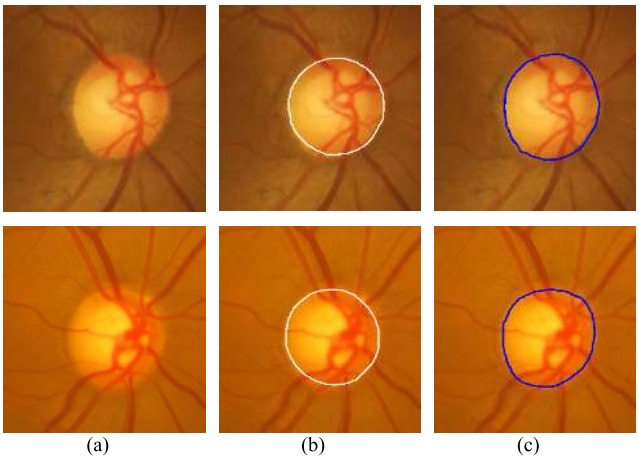

FIGURE 7. Obtaining the segmentation results of the OD. (a) Original color images; (b) the segmentation result achieved by ground truth for the OD; (c) the segmentation result achieved by proposed method for the OD.

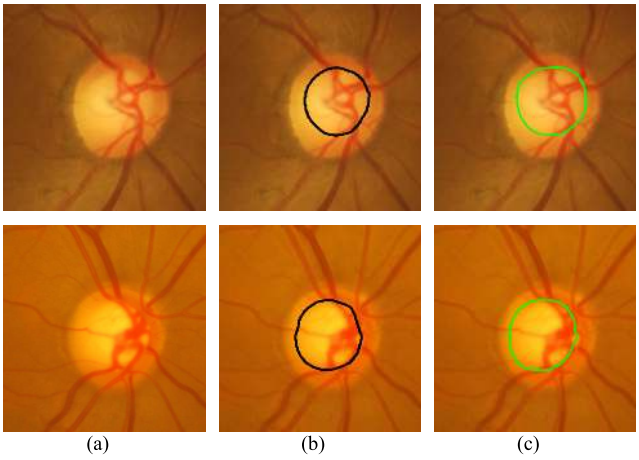

FIGURE 8. Obtaining the segmentation results of the OC. (a) Original color images; (b) the segmentation result achieved by ground truth for the OC; (c) the segmentation result achieved by proposed method for the OC.

of them bases on the overlap area between the obtained segmentation area and the ground truth area. Then, the single performance measure namely traditional F-score (F), which is the harmonic mean of precision and recall, is computed as:

$$F = 2\frac{precision \cdot recall}{precision + recall}$$

The value of F-score always lies between 0 and 1. A good segmentation performance can be indicated by a high F-score.

Second, the boundary evaluation is based on the distance between achieved boundary by method and ground truth. Let C_o be the closed boundary curves obtained by an approach and C_g be the closed boundary curves for the ground truth.

$$D = \frac{1}{k}\sum_{\theta=1}^{\theta_k}\sqrt{(d_g^\theta)^2 - (d_o^\theta)^2}$$

where d_g^θ and d_o^θ respectively indicate the distances from centroid of curve C_g to points on C_g and C_o in the angular

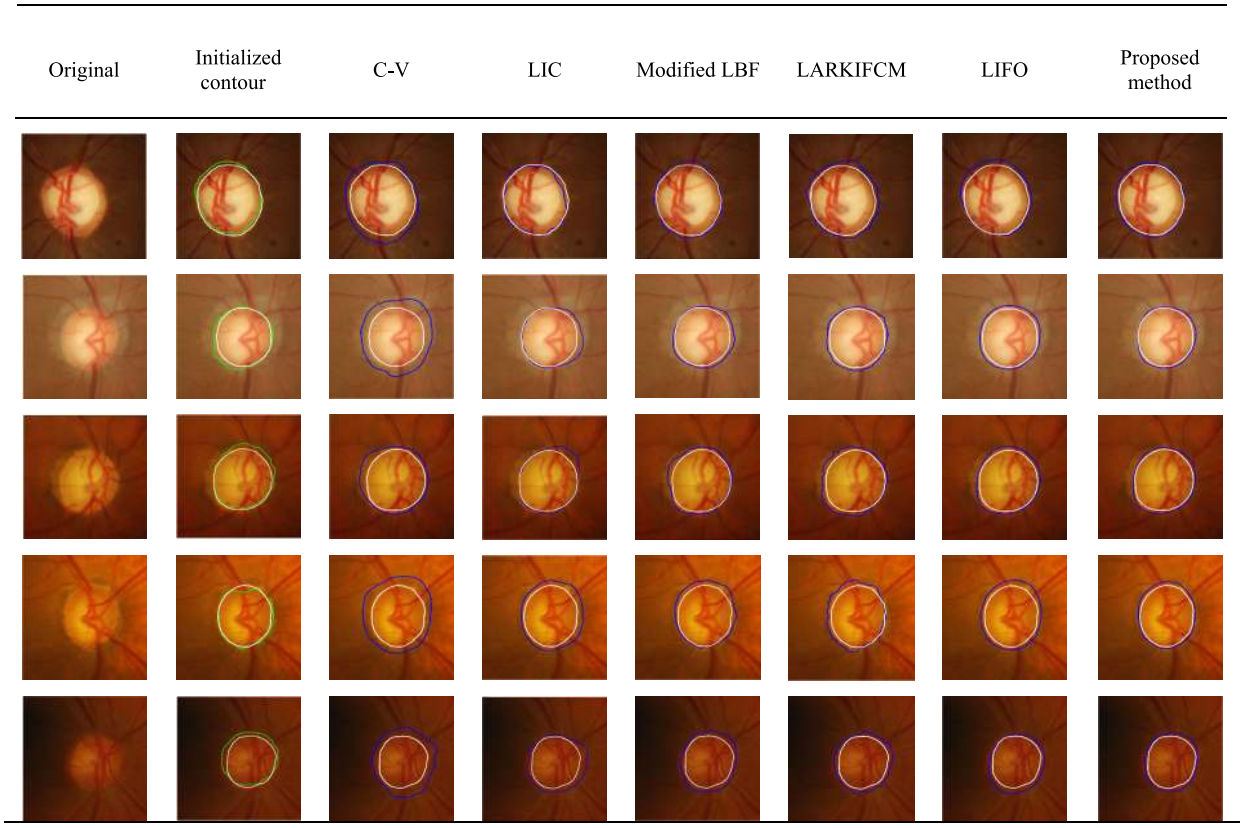

FIGURE 9. Optic disc segmentation results. First column: original images; second column: Initialized contour; third column: C-V model results [16]; fourth column: LIC model results [39]; fifth column: Modified LBF [25]; sixth column: LARKIFCM [27]; seventh column: LIFO [28]; eighth column: proposed method. White line: ground truth; blue line: detected result by an approach.

direction of θ; k expresses the total number of angular samples. In this paper, the k is set as 4 and the angular directions respectively are defined as 0^o, 90^o, 180^o and 270^o in term of [17]. Ideally, the value of D should be close to zero.

Third, the CDR estimation is based on the ratio of vertical diameters of the OD and OC areas. In Glaucoma assessment, the CDR (two standard disc parameters) is an important parameter from computing area and contour information. Here, the CDR error estimation *Error* is applied as the metric to evaluate a segmentation approach's performance. The CDR error estimation is computed as:

$$Error = |CDR_G - CDR_T|$$

where CDR_G is the result of CDR calculated from ground truth and the CDR_T is the result of CDR calculated from the obtained boundary by an approach.

D. OPTIC DISC SEGMENTATION RESULTS

Fig.9 clearly displays the results of OD segmented obtained by different common methods, in which the white lines denote the ground truth and the blue lines denote the contour achieved by the different methods. The original color image is shown in the first column and the initialized contour obtained by the aforementioned approach is in the second column. The first row illuminates a challenging situation for segmentation on an irregularly shaped OD. Comparing with the other five methods, the proposed method achieves a more complete and accurate segmentation results due to the fact that the sufficient appearance information in irregularly regions is a stronger cue than the prior shape information. The second, third and fourth row images present some segmentation results of OD which are influenced by the peripapillary atrophy (PPA). It is clearly seen that the CV model is able to extract the OD boundary and handle with the local gradient variations due to considering the global information of image, but it can't exclude the bright regions belonging to the PPA because a subtle difference presents between average intensity of the detected foreground and background regions. According to the LIC model considers the local information in a neighborhood of each point comparing with the CV model, it can achieve more accuracy segmentation result for OD. However, it fails to achieve a satisfying result since the original information in vessel-free image is neglected. The precision of the results obtained by modified LBF model exceed the one obtained by LIC due to the data obtained from multiple image planes, but it fails to deal with the appearance information missing and is influenced by the severity intensity inhomogeneity in image. The main reason is that they overlook the imperfection of the single-view information and only use the local mean information [32]. Although the LARKIFCM

TABLE 1. Optic disc segmentation results.

Methods	F-score (average)	Boundary-based distance (average)
C-V [16]	0.885	26.578
LIC [39]	0.935	11.900
Modified LBF [25]	0.941	9.510
LARKIFCM [27]	0.945	9.130
LIFO [28]	0.947	8.980
Proposed method	**0.950**	**8.320**

method can more effectively segment OD due to taking positive features of the combined approaches, it ignores the integrated information of the OD e.g. anatomical structure prior information and fails to accurately differentiate the OD region from similar regions (extremely bright region of PPA) around it. The LIFO model can overcome most of influences caused by bright regions of PPA and the OD segmentation with smooth boundary owing to constraint of shape prior. However, it is misled in some regions where shape prior information plays a leading role on account of insufficient of the intensity information. Different from these methods, the proposed approach achieves a more integrity and accuracy segmentation result due to the fact that it combines the information of appearance integrated from a multi-dimensional feature space and shape together.

In order to further evaluate the performance of these segmentation methods for the OD, Table.1 compares our method with the others in terms of F-score and boundary-based distance measures. The proposed method achieves a lower FP and FN in comparing to the other five methods due to make full use of the multi-view information based on the appearance and shape of OD and obtains the highest F-score. The average boundary distance is 8.320 achieved by the proposed method which is the lowest among all methods as segmented boundary by us is closer to the ground truth. Hence, based on the highest F-score and the lowest average boundary distance obtained by us among all the methods, the segmentation performance of our method is superior to the other methods.

E. OPTIC CUP SEGMENTATION RESULTS

In this subsection, the obvious results shown in the Fig.10 reveal that the performance of the proposed segmentation method for OC is superior to others segmentation methods such as threshold-based approach [16], ellipse fitting approach [40] and clustering-based approach [25], LARKIFCM [27]. According to the segmentation result demonstrated in the Fig.10, the OC boundary obtained by our methods has a small deviation from the ground truth both on the nasal and temporal sides. Whereas, the other methods achieve larger error referring to ground truth due to suffering a significant influence caused by dense blood vessels on the nasal side. The proposed method outperforms the other methods due to the fact that both the appearance and the shape information of OC are fully exploited. Comparing to the state-of-the-art approaches, our method presents some advantages as below: (1) The introduced LSACM can well handle the intensity inhomogeneity which is a frequently occurring phenomenon within the OC and thereby enhancing the discrimination between the OC and non-OC. (2) A novel preprocessing approach which is based on a special structure relationship for the OD and the OC is used to modify LSACM (MLSACM) to guide the OC contour evolution in an effective region. (3) The fusion of multi-aspect intensity information in the proposed model remedies the insufficient for a single-aspect intensity information, which can overcome the influence caused by vessel occlusion and reduce loss of information. (4) The proposed shape prior becomes a stronger cue than the intensity information in some region maintaining the intrinsic anatomical structure of the OC to make the contour robustly evolve found in and around objects regions. Table.2 depicts the quantitative assessment of the OC segmentation results in terms of the F-score and average boundary distance. Seen from the Table.2, it can be inferred that the proposed approach has a significant improvement in the segmentation results comparing to the other methods.

F. GLAUCOMA ASSESSMENT

According to the segmented boundary information of the OD and the OC, the cup to disc ratio (CDR) base on the vertical diameter of the OD and the OC regions (v-CDR) can be derived as the key measurement for glaucoma assessment. However, the OC may be oriented at different angles, the v-CDR measure is insufficiency. We apply the cup to disc area ratio (a-CDR) to measure overall segmentation accuracy obtained in all directions at the same time. Table.3 presents the mean error μ_{Error} and the standard deviation of the

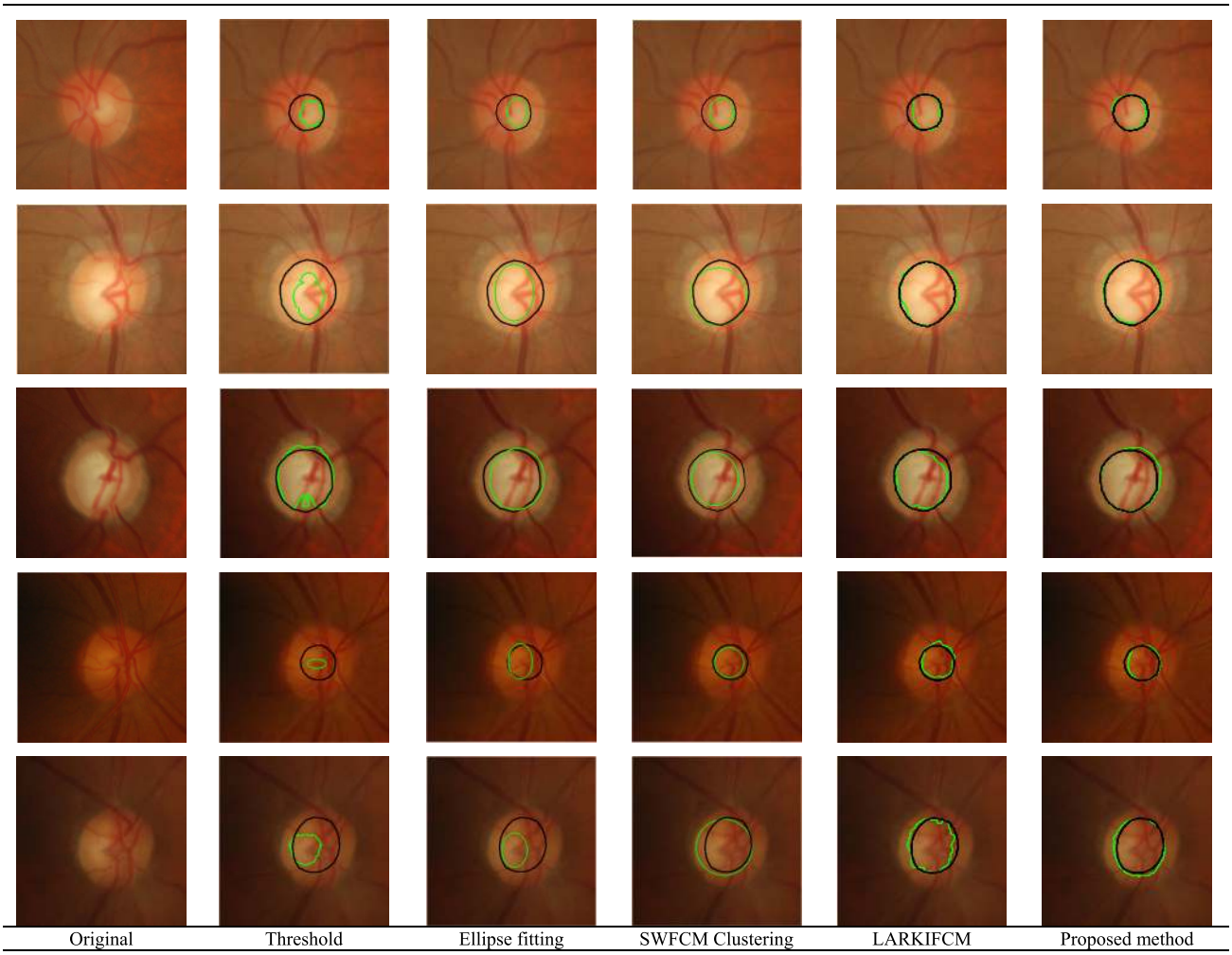

FIGURE 10. Optic cup segmentation results. First column: original images; second column: threshold-based [16]; third column: ellipse fitting [40]; fourth column: SWFCM Clustering [25]; fifth column: LARKIFCM [27]; sixth column: Proposed method. Black line: ground truth; green line: derived result by an approach.

TABLE 2. Optic cup segmentation results.

Methods	F-score (average)	Boundary-based distance (average)
Thresholding [16]	0.625	51.337
Ellipse Fitting [40]	0.659	48.783
SWFCM Clustering [25]	0.773	26.361
LARKIFCM [27]	0.816	23.144
Proposed method	**0.852**	**20.390**

TABLE 3. Error estimation in v-CDR and a-CDR (mean: μ_{Error}/standard deviation: σ_{Error}).

	Cup-to-disc vertical diameter ratio		Cup-to-disc area ratio	
	μ_{Error}	σ_{Error}	μ_{Error}	σ_{Error}
Normal images (31)	0.146	0.097	0.169	0.115
Glaucoma images (70)	0.085	0.076	0.093	0.083
Total images (101)	0.108	0.088	0.116	0.099

error σ_{Error} in estimating of the v-CDR and the a-CDR for all of the images. Comparing normal images with glaucoma images in terms of the mean error μ_{Error} and the standard deviation of the error σ_{Error}, the smaller μ_{Error} and σ_{Error} can be achieved in glaucoma images. This indicates that our method has a high sensitivity in glaucoma detection.

V. CONCLUSION

In this paper, an automated detection scheme for glaucoma in terms of different evaluation parameters was presented. These parameters require the precise segmentation information for the OD and the OC respectively obtained by two proposed methods. For extracting the accurate boundary of OD, a novel segmentation model is presented. First, LSACM is introduced to deal with the commonly occurred intensity inhomogeneity phenomenon. Then, we make full use of the multi-view information based on the appearance and shape of OD achieving accurate OD detection in varied conditions. Meanwhile, a novel OC segmentation method is also presented. First, considering the special structure relationship between the OD and the OC, a novel preprocessing approach is used to modify LSACM (MLSACM) to guide the OC contour evolution in an effective region and reduce the negative effect of non-objects, and it can overcome the difficulty which is that the traditional ACM can not directly segment the OC. Second, we extend the MLSACM model by integrating the local image probability information around the point of interest from the multi-dimensional feature space to remedy insufficient for the single-feature space. Finally, the shape priori constraint information fused in proposed model becomes a stronger cue than the intensity information in some regions maintaining the intrinsic anatomical structure of the OC. The DRISHTI-GS database is applied to evaluate the performance of two novel models for the OD and the OC. The average F-Score/average boundary distance which are 0.950/8.320 achieved by the proposed OD segmentation method and the average F-Score/average boundary distance which are 0.852/20.390 obtained by the proposed OC segmentation method are superior to ones acquired by others state-of-the-art approaches.

REFERENCES

[1] A. Chakravarty and J. Sivaswamy, "Joint optic disc and cup boundary extraction from monocular fundus images," *Comput. Methods Programs Biomed.*, vol. 147, pp. 51–61, Aug. 2017.

[2] J. Cheng, F. Yin, D. W. K. Wong, D. Tao, and J. Liu, "Sparse dissimilarity-constrained coding for glaucoma screening," *IEEE Trans. Biomed. Eng.*, vol. 62, no. 5, pp. 1395–1403, May 2015.

[3] J. Zilly, J. M. Buhmann, and D. Mahapatra, "Glaucoma detection using entropy sampling and ensemble learning for automatic optic cup and disc segmentation," *Comput. Med. Imag. Graph.*, vol. 55, pp. 28–41, Jan. 2017.

[4] M. S. Haleem, L. Han, J. V. Hemert, B. Li, A. Fleming, L. R. Pasquale, and B. J. Song, "A novel adaptive deformable model for automated optic disc and cup segmentation to aid glaucoma diagnosis," *J. Med. Syst.*, vol. 42, no. 1, p. 20, Jan. 2018.

[5] J. Cheng, J. Liu, Y. Xu, F. Yin, D. W. K. Wong, N.-M. Tan, D. Tao, C.-Y. Cheng, T. Aung, and T. Y. Wong, "Superpixel classification based optic disc and optic cup segmentation for glaucoma screening," *IEEE Trans. Med. Imag.*, vol. 32, no. 6, pp. 1019–1032, Jun. 2013.

[6] T. Damms and F. Dannheim, "Sensitivity and specificity of optic disc parameters in chronic glaucoma," *Investigative Ophthalmol. Vis. Sci.*, vol. 34, no. 7, pp. 2246–2250, Jun. 1993.

[7] N. Harizman, C. Oliveira, A. Chiang, C. Tello, M. Marmor, R. Ritch, and J. M. Liebmann, "The ISNT rule and differentiation of normal from glaucomatous eyes," *Arch. Ophthalmol.*, vol. 124, pp. 1579–1583, Nov. 2006.

[8] S. Sekhar, W. Al-Nuaimy, and A. K. Nandi, "Automated localisation of retinal optic disk using Hough transform," in *Proc. 5th IEEE Int. Symp. Biomed. Imag., (ISBI)*, May 2008, pp. 1577–1580.

[9] A. Bhuiyan, R. Kawasaki, T. Y. Wong, and R. Kotagiri, "A new and efficient method for automatic optic disc detection using geometrical features," in *Proc. World Congr. Med. Phys. Biomed. Eng.* Cham, Switzerland: Springer, 2009, pp. 1131–1134.

[10] A. Aquino, M. Emilio, E. Gegundez-Arias, and D. Marin, "Detecting the optic disc boundary in digital fundus images using morphological, edge detection, and feature extraction techniques," *IEEE Trans. Med. Imag.*, vol. 29, no. 11, pp. 1860–1869, Nov. 2010.

[11] H. Li and O. Chutatape, "Boundary detection of optic disk by a modified ASM method," *Pattern Recognit.*, vol. 36, no. 9, pp. 2093–2104, 2003.

[12] F. Yin, J. Liu, S. H. Ong, Y. Sun, D. W. K. Wong, N. M. Tan, C. Cheung, M. Baskaran, T. Aung, and T. Y. Wong, "Model-based optic nerve head segmentation on retinal fundus images," in *Proc. Annu. Int. Conf. IEEE Eng. Med. Biol. Soc.*, Aug./Sep. 2011, pp. 2626–2629.

[13] F. Yin, J. Liu, D. W. K. Wong, N. M. Tan, C. Cheung, M. Baskaran, T. Aung, and T. Y. Wong, "Automated segmentation of optic disc and optic cup in fundus images for glaucoma diagnosis," in *Proc. 25th IEEE Int. Symp. Comput.-Based Med. Syst. (CBMS)*, Jun. 2012, pp. 1–6.

[14] Y. Hatanaka, K. Fukuta, C. Muramatsu, A. Sawada, T. Hara, T. Yamamoto, and H. Fujita, "Automated measurement of cup-to-disc ratio for diagnosing glaucoma in retinal fundus images," in *Proc. World Congr. Med. Phys. Biomed. Eng.*, vol. 25, 2009, pp. 198–200.

[15] C. Muramatsu, T. Nakagawa, A. Sawada, Y. Hatanaka, T. Hara, T. Yamamoto, and H. Fujita, "Determination of cup-to-disc ratio of optical nerve head for diagnosis of glaucoma on stereo retinal fundus image pairs," *Proc. SPIE*, vol. 7260, Mar. 2009, Art. no. 72603L.

[16] G. D. Joshi, J. Sivaswamy, K. Karan, and S. R. Krishnadas, "Optic disk and cup boundary detection using regional information," in *Proc. IEEE Int. Symp. Biomed. Imag.*, Apr. 2010, pp. 948–951.

[17] G. D. Joshi, J. Sivaswamy, and S. R. Krishnadas, "Optic disk and cup segmentation from monocular color retinal images for glaucoma assessment," *IEEE Trans. Med. Imag.*, vol. 30, no. 6, pp. 1192–1205, Jun. 2011.

[18] W. W. K. Damon, J. Liu, T. N. Meng, Y. Fengshou, and W. T. Yin, "Automatic detection of the optic cup using vessel kinking in digital retinal fundus images," in *Proc. IEEE Int. Symp. Biomed. Imaging. (ISBI)*, May 2012, pp. 1647–1650.

[19] Y. Hatanaka, Y. Nagahata, C. Muramatsu, S. Okumura, K. Ogohara, A. Sawada, K. Ishida, T. Yamamoto, and H. Fujita, "Improved automated optic cup segmentation based on detection of blood vessel bends in retinal fundus images," in *Proc. 36th Annu. Int. Conf. IEEE Eng. Med. Biol. Soc.*, Aug. 2014, pp. 126–129.

[20] M. K. Dutta, A. K. Mourya, A. Singh, M. Parthasarathi, R. Burget, and K. Riha, "Glaucoma detection by segmenting the super pixels from fundus colour retinal images," in *Proc. Int. Conf. Med. Imag., M-Health Emerg. Commun. Syst. (MedCom)*, Nov. 2014, pp. 86–90.

[21] W. Zhou, S. Qiao, Y. Yi, N. Han, Y. Chen, and G. Lei, "Automatic optic disc detection using low-rank representation based semi-supervised extreme learning machine," *Int. J. Mach. Learn. Cybern.*, pp. 1–15, Jan. 2019. [Online]. Available: https://link.springer.com/article/10.1007/s13042-019-00939-0. doi: 10.1007/s13042-019-00939-0.

[22] N. M. Tan, Y. Xu, W. B. Goh, and J. Liu, "Robust multi-scale superpixel classification for optic cup localization," *Comput. Med. Imag. Graph*, vol. 40, pp. 182–193, Mar. 2015.

[23] A. Osareh, M. Mirmehdi, B. Thomas, and R. Markham, "Colour morphology and snakes for optic disc localization," in *Proc. 6th Med. Image Understand. Anal. Conf.*, Jan. 2002, pp. 21–24.

[24] S. Lankton and A. Tannenbaum, "Localizing region-based active contours," *IEEE Trans. Image Process.*, vol. 17, no. 11, pp. 2029–2039, Nov. 2008.

[25] P. S. Mittapalli and G. B. Kande, "Segmentation of optic disk and optic cup from digital fundus images for the assessment of glaucoma," *Biomed. Signal Process. Control*, vol. 24, no. 47, pp. 34–46, Feb. 2016.

[26] C. Li, C.-Y. Kao, J. C. Gore, and Z. Ding, "Implicit active contours driven by local binary fitting energy," in *Proc. IEEE Conf. Comput. Vis. Pattern Recognit.*, Jun. 2007, pp. 1–7.

[27] N. Thakur and M. Juneja, "Optic disc and optic cup segmentation from retinal images using hybrid approach," *Expert Syst. Appl.*, vol. 127, pp. 308–322, Aug. 2019.

[28] Y. Gao, X. Yu, C. Wu, W. Zhou, X. Lei, and Y. Zhuang, "Automatic optic disc segmentation based on modified local image fitting model with shape prior information," *J. Healthcare Eng.*, vol. 2019, Mar. 2019, Art. no. 2745183.

[29] W. Zhou, C. Wu, Y. Gao, and X. Yu, "Automatic optic disc boundary extraction based on saliency object detection and modified local intensity clustering model in retinal images," *IEICE Trans. Fundam. Electron., Commun. Comput. Sci.*, vols. E100–A, no. 9, pp. 2069–2072, 2017.

[30] Y. Qin, H. Lu, Y. Xu, and H. Wang, "Saliency detection via cellular automata," in *Proc. IEEE Conf. Comput. Vis. Pattern Recognit. (CVPR)*, Jun. 2015, pp. 110–119.
[31] J. Liu, D. W. K. Wong, J. H. Lim, X. Jia, F. Yin, H. Li, W. Xiong, and T. Y. Wong, "Optic cup and disk extraction from retinal fundus images for determination of cup-to-disc ratio," in *Proc. IEEE Conf. Ind. Electron. Appl.*, Jun. 2008, pp. 1828–1832.
[32] K. Zhang, L. Zhang, K.-M. Lam, and D. Zhang, "A level set approach to image segmentation with intensity inhomogeneity," *IEEE Trans. Cybern.*, vol. 46, no. 2, pp. 546–557, Feb. 2016.
[33] A. Li, Z. Niu, J. Cheng, F. Yin, D. W. K. Wong, S. Yan, and J. Liu, "Learning supervised descent directions for optic disc segmentation," *Neurocomputing*, vol. 275, pp. 350–357, Jan. 2018.
[34] P. Ganesan, K. B. Shaik, B. S. Sathish, and V. Kalist, "Neural network based SOM for multispectral image segmentation in RGB and HSV color space," in *Proc. Int. Conf. Circuits, Power Comput. Technol. (ICCPCT)*, Mar. 2015, pp. 1–6.
[35] M. S. Haleem, L. Han, J. van Hemert, and B. Li, "Automatic extraction of retinal features from colour retinal images for glaucoma diagnosis: A review," *Comput. Med. Imag. Graph.*, vol. 37, nos. 7–8, pp. 581–596, Oct./Dec. 2013.
[36] M. Esmaeili, H. Rabbani, and A. M. Dehnavi, "Automatic optic disk boundary extraction by the use of curvelet transform and deformable variational level set model," *Pattern Recogn.*, vol. 45, no. 7, pp. 2832–2842, Jul. 2012.
[37] F. Khan, S. A. Khan, U. U. Yasin, I. U. Haq, and U. Qamar, "Detection of glaucoma using retinal fundus images," in *Proc. Int. Conf. Robot. Emerg. Allied Technol. Eng. (iCREATE)*, Apr. 2014, pp. 1–5.
[38] J. Sivaswamy, S. R. Krishnadas, G. D. Joshi, M. Jain, and A. U. S. Tabish, "Drishti-GS: Retinal image dataset for optic nerve head(ONH) segmentation," in *Proc. IEEE 11th Int. Symp. Biomed. Imag. (ISBI)*, Apr./May 2014, pp. 53–56.
[39] C. Li, R. Huang, Z. Ding, J. C. Gatenby, D. N. Metaxas, and J. C. Gore, "A level set method for image segmentation in the presence of intensity inhomogeneities with application to MRI," *IEEE Trans. Image Process.*, vol. 20, no. 7, pp. 2007–2016, Jul. 2011.
[40] J. Liu, D. Wong, J. Lim, H. Li, N. Tan, and T. Wong, "Argali: An automatic cup to disc ratio measurement system for glaucoma detection and analysis framework," *Proc. SPIE*, vol. 7260, Feb. 2009, Art. no. 72603K.

YUAN GAO received the M.S. degree in control science and engineering from Shenyang University, in 2016. He is currently pursuing the Ph.D. degree with Northeastern University, Shenyang, China. His research interests include medical imaging processing, machine learning, and pattern recognition.

XIAOSHENG YU received the M.S. degree from the University of Liverpool, in 2007, and the Ph.D. degree in pattern recognition and intelligent system from Northeastern University, in 2014, where he is currently a Lecturer with the Faculty of Robot Science and Engineering. His main research interests include image processing, machine learning, pattern recognition, and wireless sensor networks.

CHENGDONG WU is currently the Vice President of the Faculty of Robot Science and Engineering, Shenyang Northeastern University, the Director of the Institute Artificial Intelligence, a Professor, and the Doctoral tutor with Northeastern University, Shenyang, China. He has long been involved in automation engineering, artificial intelligence and teaching, and researching in robot navigation. He is an expert of the Chinese modern artificial intelligence and robot navigation, and he is also the Special Allowance of the State Council.

WEI ZHOU received the Ph.D. degree from Northeastern University, in 2018. She is currently a Lecturer with the School of Computing, Shenyang Aerospace University. Her main research interests include imaging processing, dimensionality reduction, and feature selection.

XIAONAN WANG received the Ph.D. degree from the China Medical University, in 2019, where she is currently a Lecturer. Her research interests include clinical oncotherapy and antitumor immunity.

HAO CHU received the Ph.D. degree from Northeastern University, Shenyang, China, in 2017. Since 2006, she has been with the Faculty of Robot Science and Engineering, College of Information Science and Engineering, Northeastern University. Her research interests include imaging processing, robot navigation, and localization algorithm in the wireless sensor networks.